Unveiling the "invisible" druggable conformations of GDP-bound inactive Ras

Dan Liu[a,1], Yunyun Mao[a,1], Xue Gu[a], Yang Zhou[a], and Dong Long (龙冬)[a,b,2]

[a]Hefei National Laboratory for Physical Sciences at the Microscale, MOE Key Laboratory for Membraneless Organelles and Cellular Dynamics, and School of Life Sciences, University of Science and Technology of China, Hefei 230027, China; and [b]Department of Chemistry, University of Science and Technology of China, 230026 Hefei, China

Edited by Lewis E. Kay, University of Toronto, Toronto, Canada, and approved February 6, 2021 (received for review December 1, 2020)

The prevalent view on whether Ras is druggable has gradually changed in the recent decade with the discovery of effective inhibitors binding to cryptic sites unseen in the native structures. Despite the promising advances, therapeutics development toward higher potency and specificity is challenged by the elusive nature of these binding pockets. Here we derive a conformational ensemble of guanosine diphosphate (GDP)-bound inactive Ras by integrating spin relaxation-validated atomistic simulation with NMR chemical shifts and residual dipolar couplings, which provides a quantitative delineation of the intrinsic dynamics up to the microsecond timescale. The experimentally informed ensemble unequivocally demonstrates the preformation of both surface-exposed and buried cryptic sites in Ras•GDP, advocating design of inhibition by targeting the transient druggable conformers that are invisible to conventional experimental methods. The viability of the ensemble-based rational design has been established by retrospective testing of the ability of the Ras•GDP ensemble to identify known ligands from decoys in virtual screening.

conformational ensemble | spin relaxation | residual dipolar coupling | chemical shift | virtual screening

Situated in a central position of the complex intracellular signaling network, Ras proteins play critical roles in regulating cell growth, differentiation, migration and apoptosis through cycling between the guanosine diphosphate (GDP)-bound inactive and guanosine triphosphate (GTP)-bound active forms (1, 2). Aberrant signaling caused by oncogenic mutations in Ras that break this physiological balance can result in uncontrolled cell proliferation and ultimately the development of human malignancies (3, 4). Despite its well-established role in tumorigenesis and the extensive efforts to target this oncoprotein in past decades, clinically approved therapies remain unavailable. One obstacle to the development of anti-Ras drugs lies in the native structures of active and inactive Ras that lack apparently druggable pockets for high-affinity interactions with inhibitory compounds (5–7).

Both the active and inactive forms of Ras, however, are inherently flexible, populating rare conformers distinct from the native structures and presenting alternative opportunities for drug discovery (8–11). For example, in GTP-bound active Ras, a major and minor state (termed states 2 and 1, respectively) coexist in solution and exchange on a millisecond timescale, with state 1 showing surface roughness unobserved in the major state (12–18). The direct visibility of state 1 in the one-dimensional ^{31}P NMR spectra of active Ras largely facilitated its early discovery and characterization (12, 19). And the available mutants of H-Ras (e.g., T35A), or the homolog M-Ras, which predominantly assume the state 1 conformation, further promoted the atomic-resolution studies of its structure and internal dynamics, as well as the concomitant drug discovery efforts targeting this low-populated conformer (17, 18, 20).

In comparison to the intensive studies on active Ras, research on the dynamics of GDP-bound inactive Ras has lagged far behind, presumably due to its high degree of spectral homogeneity with little sign of resonance splitting or exchange broadening at room temperature (21). The previously reported cryptic pockets for covalent and noncovalent inhibitors of Ras•GDP (22–24), which are unseen in the compound-free structure, nevertheless indicate that the inactive form is also structurally plastic. The recent relaxation-based NMR experiments carried out at low temperature successfully captured the intrinsic microsecond timescale motions in Ras•GDP, which map to regions that overlap with those rearranged on the binding of inhibitors (11). However, the structural information of the transiently formed excited state, in the form of chemical shifts, is not available from the relaxation measurements, owing to the fast exchange rate on the chemical shift timescale. Moreover, unlike the case of active Ras, there are no known mutations that can stabilize the excited state of Ras•GDP for investigations using conventional biophysical techniques. Thus far, the sparsely populated conformations of inactive Ras derived from its microsecond dynamics remain poorly understood, precluding structure-based rational drug discovery.

To address these challenges, in this work we constructed a solution ensemble of Ras•GDP by integrating atomistic computer simulation with diverse NMR experimental parameters containing complementary information about the intrinsic protein motions on timescales from picoseconds to microseconds. This NMR-based ensemble well covers the slow dynamics as probed by spin relaxation and provides an atomic-resolution delineation of thermally accessible conformations, including

Significance

Recent progress in targeting Ras, an oncoprotein involved in approximately 30% of all human cancers, has been made with the identification of covalent and noncovalent inhibitors binding to druggable pockets that are not observed in the inhibitor-free protein structures. To understand the nature of these cryptic sites and to facilitate rational drug discovery, we constructed a conformational ensemble of inactive Ras by exploiting the rich information on protein intrinsic dynamics provided by NMR experimental and computational approaches. Our results unveil the transiently sampled conformations bearing preformed druggable pockets and demonstrate the utility of the Ras•GDP ensemble for computer-aided drug design.

Author contributions: D. Long designed research; D. Liu, Y.M., X.G., Y.Z., and D. Long performed research; D. Liu and Y.M. analyzed data; and D. Liu, Y.M., and D. Long wrote the paper.

The authors declare no competing interest.

This article is a PNAS Direct Submission.

[1]D. Liu and Y.M. contributed equally to this work.

[2]To whom correspondence may be addressed. Email: dlong@ustc.edu.cn.

This article contains supporting information online at https://www.pnas.org/lookup/suppl/doi:10.1073/pnas.2024725118/-/DCSupplemental.

Published March 8, 2021.

those bearing surface or buried pockets similar to the cryptic pockets previously observed in the inhibitor-bound forms. The utility of the Ras•GDP ensemble in the development of inhibitors is demonstrated by ensemble-based virtual screening, which achieves an impressive level of enrichment of known binders.

Results

Spin-Relaxation Active Slow Motions Sampled by Extended Molecular Dynamics Simulation. Slow molecular motions on the microsecond timescale that stochastically modulate isotropic chemical shifts can contribute to detectable spin relaxation, based on which the exchange correlation time (τ_{ex}) of Ras•GDP was previously determined to be 34 μs at 5 °C (11). To further probe the temperature influence on the slow dynamics, in this work we measured the relaxation rates of four bilinear coherences—$2H_zN_z$, $2H_xN_z$, $2H_zN_x$, and $2H_xN_x$—for Ras•GDP at 22 °C, from which the ^{15}N relaxation rates (R_{ex}) contributed by microsecond motions were quantified (details in *SI Appendix*). As shown in Fig. 1*A*, the increase in temperature markedly reduced the magnitudes of R_{ex} and thereby significantly accelerated the protein motions (as τ_{ex} scales with R_{ex} in the fast-exchange time regime).

To computationally capture the relaxation-active slow dynamics, a 10-μs all-atom simulation of Ras•GDP was carried out using the Amber ff14SB force field (25) and explicit solvent model at 300 K (27 °C). From the extended molecular dynamics (MD) trajectory, the R_{ex} rates contributed by fast exchange were back-calculated using the autocorrelation function of time-dependent chemical shift variations (26, 27),

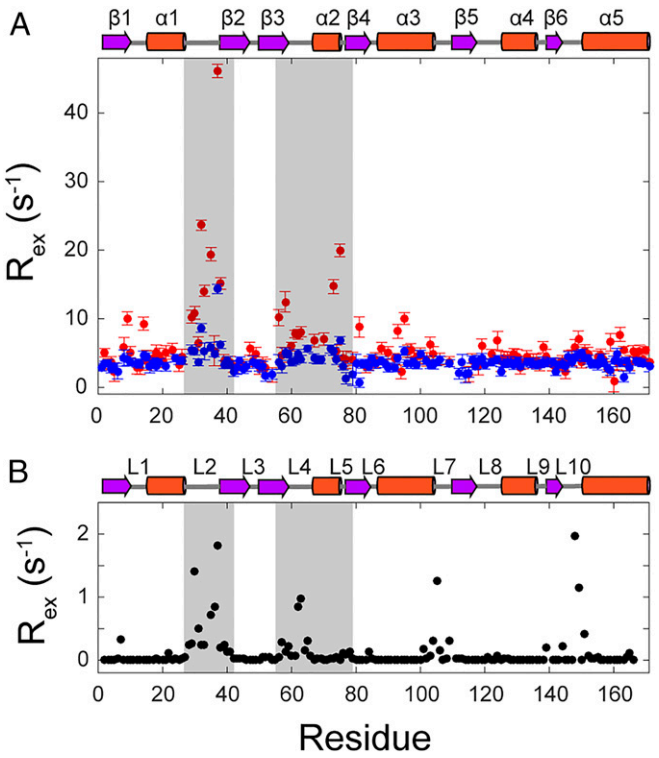

Fig. 1. Transverse relaxation rates (R_{ex}) of ^{15}N contributed by microsecond timescale dynamics. (*A*) The experimental R_{ex} values for Ras•GDP at 5 °C (red) and 22 °C (blue) were determined by measuring the relaxation rates of $2H_zN_z$, $2H_xN_z$, $2H_zN_x$, and $2H_xN_x$ with spin lock fields (details in *SI Appendix*). The data at 5 °C are taken from our previous work (11). The shaded areas highlight the regions with significant exchange-induced relaxation. (*B*) R_{ex} rates back-calculated from the 10-μs MD trajectory at 27 °C.

$$R_{ex} = (\gamma_N B_0)^2 \int_0^\infty \{\langle \delta(t)\delta(t+\tau)\rangle - \langle\delta\rangle^2\} d\tau \quad [1]$$

where γ_N is the ^{15}N gyromagnetic ratio, B_0 is the static field strength, and the angular bracket denotes ensemble averaging. The chemical shifts, $\delta(t)$, for each snapshot were predicted using SPARTA+ (28). As shown in Fig. 1*B*, the exchange-induced relaxation in regions including switch I and II (residues 30 to 38 and 60 to 76) is well reproduced by the in silico simulation, while the back-calculated R_{ex} values (<2 s^{-1}) are smaller than the experimental values, which is attributable in part to the higher temperature used for the simulation. It is interesting to note that the residues around loops L7 and L10 also showed relatively large R_{ex} in the simulation. These residues do not have quantifiable R_{ex} from the NMR relaxation measurements; however, the small increase in the crystallographic B-factors in these regions is consistent with their flexibility (Fig. 2*G*). As R_{ex} values are highly sensitive to the motional timescales, this result indicates that the energy barriers (kinetics) for these residues are overestimated in ff14SB. The actual correlation times for these residues are expected to be faster than microseconds, which diminishes the integral in Eq. **1**. Yet the large structural pool generated by the extended simulation provides a favorable starting point for subsequent experimentally guided ensemble construction.

The Ensemble of Inactive Ras Determined with NMR Chemical Shifts and RDCs. Chemical shifts and residual dipolar couplings (RDCs) are both sensitive to protein motions on microsecond and faster timescales and reflect complementary information on structural fluctuations. While RDCs report on bond vector orientations, chemical shifts correlate with a set of structural factors, including torsion angles, hydrogen bonds, electric fields, ring-current effects, et cetera. To accurately describe the thermally accessible conformational space of Ras•GDP in solution, the experimental ^{13}Cα, ^{13}Cβ, ^{13}C′, and ^{15}N chemical shifts and one-bond ^{1}H-^{15}N RDCs in three alignment media were used conjointly for selecting an ensemble of Ras•GDP from the 10-μs MD pool using a genetic-algorithm based approach (details in *SI Appendix*). The resulting ensemble, $E_{NMR,\mu s}$, comprising 128 conformers, achieves excellent agreement with the experimental data, with chemical shift root mean square deviations of 0.85 ppm (^{13}Cα), 0.99 ppm (^{13}Cβ), 0.93 ppm (^{13}C′), and 2.39 ppm (^{15}N) and the average RDC Q value of 0.139 (Fig. 2 *A*–*E*). To assess the robustness of the numerical optimization, a 10-fold cross-validation, in which 10% of the experimental data were left out as the testing data set in each of the 10 iterations, was performed. The highly comparable results obtained for the training and testing datasets (*SI Appendix*, Fig. S8) attest to the robustness of the ensemble refinement; details of the validation are provided in *SI Appendix*.

To further evaluate the quality of the chemical shifts and RDCs-derived model, we cross-checked $E_{NMR,\mu s}$ against the nuclear Overhauser effects (NOEs) (29) and isotropic crystallographic B-factors (30) of Ras•GDP that were not included as restraints for generating the ensemble. Remarkably, quantitative agreement with the experimental NOEs is achieved with no distance violations larger than 1 Å (*SI Appendix*, Table S1), and a consistent pattern found between the back-calculated and experimental B-factors with Pearson correlation coefficients of 0.62 and 0.92 including and excluding the switch I region (residues 25 to 40), respectively (Fig. 2*G*). The different B-factor patterns in the switch I region are likely caused by the crystal contact effects (31, 32), which are known to significantly affect the motion of flexible residues. The overall smaller magnitudes of experimental than predicted B-factors throughout the entire protein sequence are attributed to the cryogenic temperature (100 K) for the data collection (33, 34).

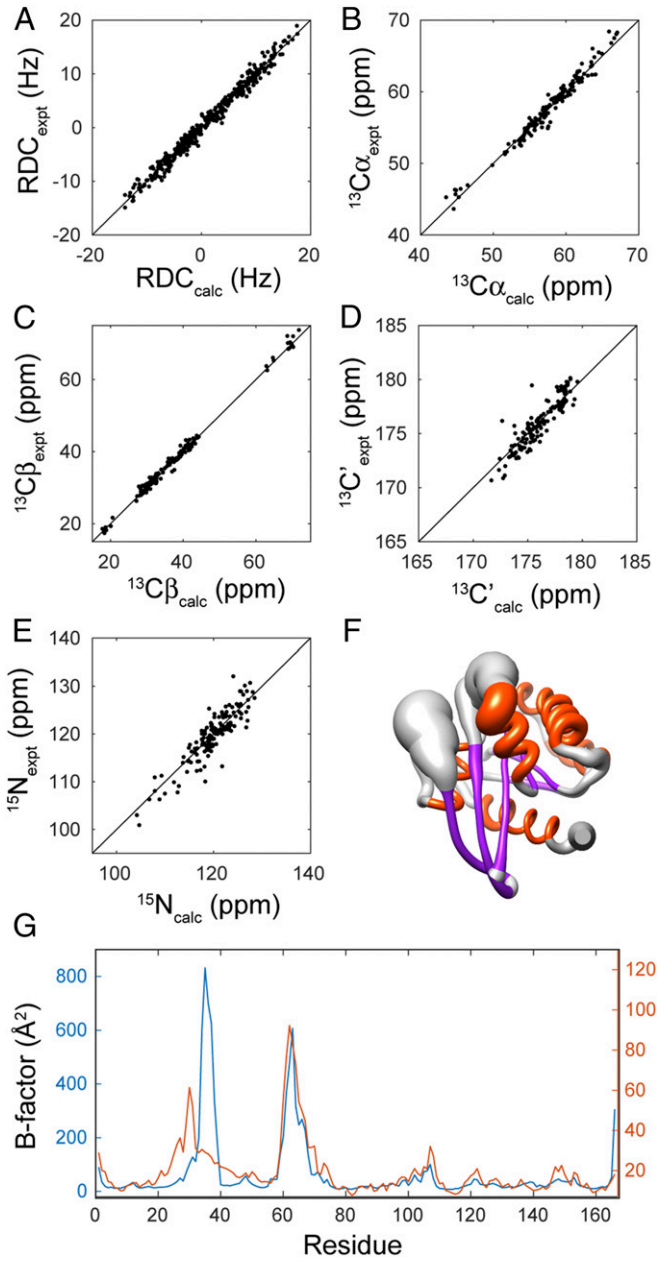

Fig. 2. The NMR-derived Ras•GDP ensemble. (*A*–*E*) The experimental RDCs (*A*) and ^{13}Cα (*B*), ^{13}Cβ (*C*), ^{13}C′ (*D*), and ^{15}N (*E*) chemical shifts vs. those back-calculated from $E_{NMR,\mu s}$. (*F*) The sausage representation of the $E_{NMR,\mu s}$ ensemble with radii showing the average deviations of Cα atoms from the mean structure. The α-helices and β-sheet are colored orange and purple, respectively. (*G*) Comparison of the crystallographic B-factors of Ras•GDP (PDB ID code 5W22; orange) with those back-calculated from $E_{NMR,\mu s}$ (blue).

Preformed Cryptic Pockets in the Unbound Protein Revealed by $E_{NMR,\mu s}$. Recent efforts to directly inhibit Ras (22–24) led to identification of cryptic sites that are barely visible in the unbound structures. The binding pocket located beneath the switch II region (hereinafter referred to as SII-P) accommodates the G12C mutant-specific covalent inhibitors, while a set of noncovalent inhibitors can bind to another site between the α2 helix and central β-sheet (hereinafter referred to as SI/II-P). The hidden nature of these pockets, however, presents significant challenges for inhibitor design through analysis of target conformations.

Two classical models, "conformational selection" and "induced fit" in which bound conformations exist prior to or are induced by the binding event, respectively (35–39), can provide potential explanations for binding at cryptic sites. To elucidate the mechanism of inhibitor recognition, the thermally accessible conformations of Ras•GDP manifested by $E_{NMR,\mu s}$ were examined in detail, revealing that both SI/II-P and SII-P are preformed in the compound free protein (Fig. 3). This result is particularly unanticipated for SII-P that is structurally buried beneath the switch II region and widely assumed to be induced by the covalent bonding (40–43). Instead, $E_{NMR,\mu s}$ shows that SII-P is readily preformed without any compounds and is highly flexible, with volumes fluctuating from 0 to ~1,100 Å^3 and surface areas ranging from 0 to ~600 Å^2, which can be significantly larger than SI/II-P. For the latter, the volumes and surface areas are up to ~800 Å^3 and ~300 Å^2, respectively. Fig. 3 *C*–*F* compares the distributions of different pocket descriptors for SI/II-P and SII-P in $E_{NMR,\mu s}$ with the experimental structures of Ras•GDP complexed with SI/II-P or SII-P inhibitors. Notably, the conformational heterogeneities of both pockets in $E_{NMR,\mu s}$ suffice to explain those observed in the complexed forms,

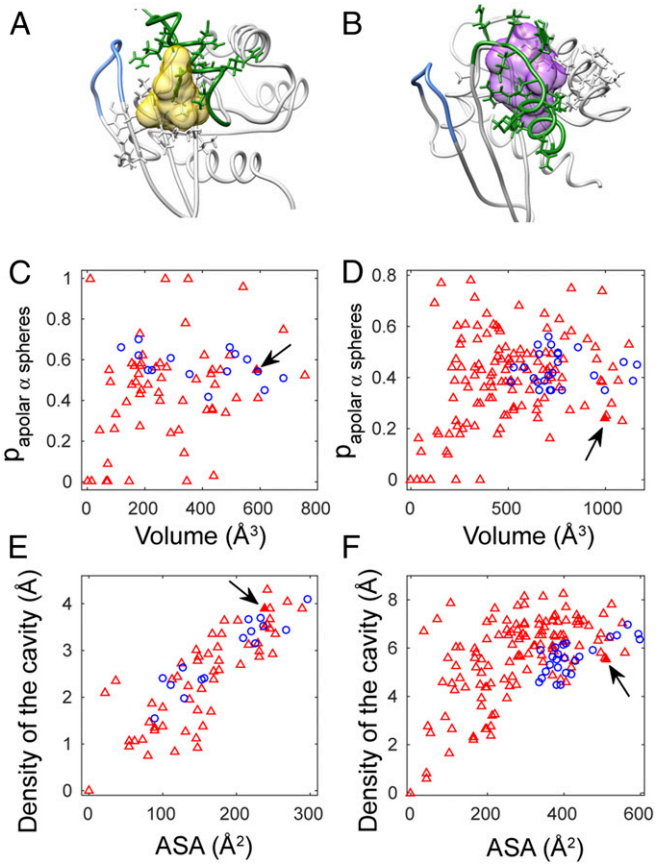

Fig. 3. Characterizations of preformed SI/II-P and SII-P in $E_{NMR,\mu s}$. (*A* and *B*) Representative structures from $E_{NMR,\mu s}$ with preformed SI/II-P and SII-P that are indicated by yellow (*A*) and purple (*B*) semitransparent surfaces, respectively. The switch I and II regions are colored in blue and green, respectively. (*C*–*F*) Distributions of pocket volumes, proportions of apolar α spheres ($p_{apolar\ \alpha\ spheres}$), density of the cavity, and accessible surface areas (ASA) of SI/II-P (*C* and *E*) and SII-P (*D* and *F*) in $E_{NMR,\mu s}$ (red triangles). The corresponding descriptors for experimentally solved Ras•GDP structures (blue circles; PDB codes in *SI Appendix*) complexed with SI/II-P or SII-P inhibitors are shown in panels *C*, *E* and *D*, *F*, respectively, for comparison. The pocket descriptors for the SI/II-P (SII-P) displayed in *A* (*B*) are denoted by the filled red triangles in *C* and *E* (*D* and *F*) and indicated by black arrows.

supporting the conformational selection mechanism for the ligand recognition processes. The central idea of conformational selection that bound structures are captured by ligands from the preformed ensemble signifies the feasibility of $E_{NMR,\mu s}$-based drug discovery.

Ensemble-Based Virtual Screening. As a proof-of-concept study, we carried out ensemble-based virtual screening (EBVS) of compound libraries comprising both known inhibitors of Ras•GDP and property-matched decoys against $E_{NMR,\mu s}$ for a retrospective assessment of its ability to enrich the experimentally verified ligands. The protocol of the enhanced directory of useful decoys (DUD-E) (44) was used to generate optimal decoy sets for the computational testing, which are physicochemically similar to but topologically distinct from the ligand sets. The experimental structures of Ras•GDP that were solved with inhibitors bound to SI/II-P (or SII-P) were assembled as a benchmark ensemble, $E_{BM,SI/II-P}$ (or $E_{BM,SII-P}$), for assessing the performance of $E_{NMR,\mu s}$, the former representing a "true" solution of the selected conformations.

For EBVS against the SI/II-P, 17 experimentally verified ligands (*SI Appendix*, Fig. S9), including 4 for which the complex structures are unavailable, and 850 DUD-E derived decoys were docked to both $E_{NMR,\mu s}$ and $E_{BM,SI/II-P}$. The ligand enrichment levels are illustrated with the receiver operating characteristic (ROC) curves that plot the true-positive rates (TPR) versus false-positive rates (FPR) (Fig. 4*A*), and the area under the ROC curve (AUC) is used as a metric for evaluation, where an AUC of 1 (≤0.5) indicates perfect (no) enrichment of known binders. Remarkably, the AUC for $E_{NMR,\mu s}$ (0.719) reached a value equivalent to or better than that of $E_{BM,SI/II-P}$ (0.705), suggesting that $E_{NMR,\mu s}$ attains the accuracy that can quantitatively support drug discovery targeting this cryptic site.

The performance of $E_{NMR,\mu s}$ in EBVS was further compared to that of the crystal structure of Ras•GDP (Protein Data Bank [PDB] ID code 4Q21), as well as a 128-conformer ensemble, E_{rand}, selected at random from the 10-μs MD pool. This crystal structure was used as the starting conformation for the MD simulation and represents the ground state without the cryptic binding site. Serving as a negative control, it shows an AUC of 0.559 with essentially no selectivity of the ligands. On the other hand, E_{rand}, with an AUC of 0.671 that indicates enrichment, represents the unweighted conformational space sampled by the unrestrained MD trajectory (*SI Appendix*, Fig. S5). Its lower level of enrichment than that of $E_{NMR,\mu s}$ demonstrates the improved accuracy of $E_{NMR,\mu s}$ over the original MD ensemble.

In contrast to the case of SI/II-P, the binding energy to SII-P was previously shown to be contributed primarily by the covalent bonding, while noncovalent interactions are weak (41, 45). To evaluate the noncovalent effects, we construct a compound library comprising the moieties of known ligands (*SI Appendix*, Fig. S10), which fit into the pocket and exclude the electrophilic warheads, and property-matched decoys generated with the DUD-E procedure. Docking of this library to $E_{BM,SII-P}$ resulted in an ROC curve with an AUC of 0.547 (Fig. 4*D*), showing that the experimentally determined bound conformations are unable to distinguish ligands from decoys. A similarly low AUC (0.534) was also obtained for $E_{NMR,\mu s}$. This result confirms the insignificant noncovalent effects for current SII-P inhibitors and points out the potential to further enhance their potency and specificity by optimizing these interactions.

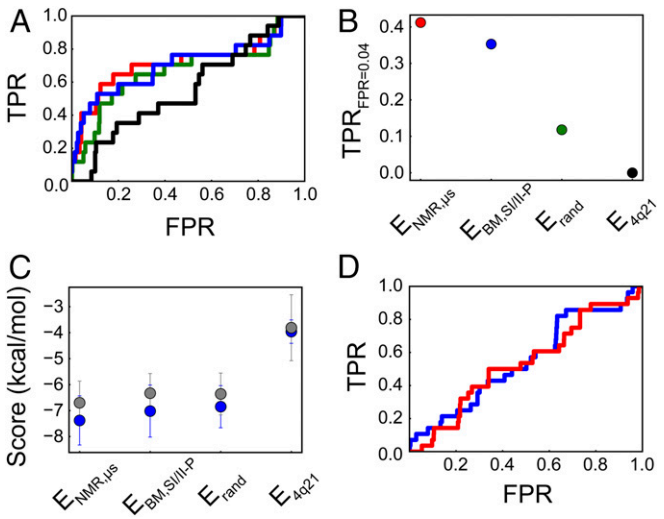

Fig. 4. Enrichment of known inhibitors in ensemble-based virtual screenings. (*A*) ROC curves showing enrichment of SI/II-P inhibitors in EBVS against $E_{NMR,\mu s}$ (red), $E_{BM,SI/II-P}$ (blue), E_{rand} (green), and the inhibitor-free crystal structure E_{4q21} (black). (*B*) True-positive rates of SI/II-P ligands in EBVS against individual ensembles when 4% of decoys were screened (FPR = 0.04). (*C*) Average docking scores and SDs (indicated by the error bars) for known ligands (blue) and decoys (gray) in EBVS against the SI/II-P of individual ensembles. (*D*) ROC curves for EBVS against the SII-P of $E_{NMR,\mu s}$ (red) and $E_{BM,SII-P}$ (blue).

Discussion

It has been shown by growing evidence that "invisible" excited conformations of proteins, which deviate from native structures and are accessed by thermal motions, are critical for recognition of physiological ligands as well as drugs that can effectively modulate protein activities. The high-resolution crystal structures of Ras have been available since the 1990s (6, 7, 46), but did not reveal suitable sites for small-molecule binding, making this oncoprotein long considered "undruggable." Thus, exploring alternative local energy minima, which transient druggable conformations could populate, for ligand design is of great interest. Central to this approach, however, is the quantitative modeling of the sparsely populated conformations at the atomic level, which can afford subsequent computer-aided drug design. The previously detected microsecond dynamics of Ras•GDP by spin relaxation (11) supports the idea of targeting the rare conformers. However, in a fast exchange system, as in the case of inactive Ras, the site-specific chemical shift information cannot be unambiguously determined, obstructing the structural understanding of the excited state.

To address this problem, we sought to complement NMR experimental data with explicit computer simulation. The latter, with the advancement of computer power, has now been able to reach the microsecond-millisecond time window. However, integrative studies combining experimental and computational tools to explore protein slow dynamics on this timescale remain scarce. In this work, we demonstrate that the extended MD simulation with the state-of-the-art force field can semiquantitatively reproduce the exchange-broadening effects observed in inactive Ras, thereby uncovering its accessible conformational space, albeit imprecisely weighted (*SI Appendix*, Figs. S5 and S6). Further optimization against a large set of RDCs and chemical shifts, which are increasingly used as exclusive or complementary restraints for determining protein structures and dynamics (47–50), yields a highly accurate ensemble, $E_{NMR,\mu s}$, consistent with diverse types of experimental parameters (Fig. 2 and *SI Appendix*, Table S1). The integrated ensemble modeling as implemented in this work demonstrates a general approach that can overcome the technical challenge of characterizing relaxation-active microsecond timescale dynamics at atomic resolution.

The mechanisms of how cryptic sites form would have important implications for the strategies for targeting them. For SII-P, which is much more buried than SI/II-P and found to

accommodate only allele-specific covalent inhibitors, the "induced fit" model has been commonly assumed. Nevertheless, the $E_{NMR,\mu s}$ ensemble of Ras•GDP unequivocally shows that the formation of both cryptic pockets, SI/II-P and SII-P, is independent of the ligands, and that their conformational heterogeneity well accounts for the diverse pocket structures observed in the complexes, supporting the conformational selection as the primary mechanism for both pockets. In the scenario of conformational selection, the intrinsic dynamics of macromolecules dictate the accessible conformations from which a ligand can select, highlighting the predictability and designability of inhibitory compounds based on the unbound protein ensembles. To prove this feasibility, we conducted comparative virtual screenings against different Ras•GDP ensembles. For both SI/II-P and SII-P, the performance of $E_{NMR,\mu s}$ matches that of the benchmark ensembles, with equally high and low AUCs for SI/II-P and SII-P, respectively, attesting to the overall accuracy of $E_{NMR,\mu s}$ and pointing out that the potencies of SII-P inhibitors can be further improved via optimization of noncovalent interactions. It is noteworthy that the druggable conformations of Ras•GDP unveiled by $E_{NMR,\mu s}$ far exceed what have been known from the Ras-inhibitor complex structures. Apart from retrospective studies, $E_{NMR,\mu s}$ is expected to significantly expedite the prospective discovery of novel inhibitors via both virtual screening and de novo design.

Materials and Methods

Sample Preparation. The uniformly ^{15}N- and $^{13}C,^{15}N$-labeled samples of human H-Ras (residues 1 to 166), as well as the perdeuterated (U-$^{2}H,^{15}N$-labeled) sample (residues 1 to 171), were expressed and purified as described previously (21, 51). The buffer for all NMR samples contained 20 mM Tris pH 7.5, 100 mM NaCl, 5 mM $MgCl_2$, 1 mM DTT, 0.01% sodium azide, and 10% D_2O. Residual dipolar couplings were measured in three alignment media: 1) 17 mg/mL Pf1 phage (52); 2) sodium octyl sulfate (SOS)-doped PEG bicelle (53), with 4.2% (wt/vol) $C_{12}E_5$ and molar ratios of $C_{12}E_5$/hexanol and $C_{12}E_5$/SOS of 0.96:1 and 30:1, respectively; and 3) negatively charged stretched gel, which was polymerized with 2.33% (wt/vol) acrylamide, 2.44% (wt/vol) 2-acrylamido-2-methyl-1-propanesulfonic acid, 0.23% (wt/vol) N,N′-methylenebisacrylamide, 0.1% ammonium persulfate, and 0.05% tetramethylethylenediamine. After thorough washing and drying, the gel was swelled in the protein solution within the chamber of a gel stretcher (54). The diameter of the stretched gel changed from 6 mm to 4.2 mm. The RDCs obtained in media 1 and 3 are largely correlated, thereby providing limited complementary information to each other. Medium 2, on the other hand, produced a considerably different alignment (*SI Appendix*, Fig. S4).

NMR experiments, ensemble modeling, validation, analyses, and ensemble-based virtual screening are described in detail in *SI Appendix*.

Data Availability. All study data are included in the main text and/or *SI Appendix*.

ACKNOWLEDGMENTS. We acknowledge the use of computing resources at the Supercomputing Center of University of Science and Technology of China. This work was supported by the National Key R&D Program of China (2016YFA0501202, to D. Long), the National Natural Science Foundation of China (21822406 and 22074134, to D. Long and 31900860, to Y.M.), and the Provincial Natural Science Foundation of Anhui (2008085MC64, to Y.M.).

1. I. R. Vetter, A. Wittinghofer, The guanine nucleotide-binding switch in three dimensions. *Science* **294**, 1299–1304 (2001).
2. D. S. Goodsell, The molecular perspective: The ras oncogene. *Oncologist* **4**, 263–264 (1999).
3. D. Hanahan, R. A. Weinberg, The hallmarks of cancer. *Cell* **100**, 57–70 (2000).
4. D. Vigil, J. Cherfils, K. L. Rossman, C. J. Der, Ras superfamily GEFs and GAPs: Validated and tractable targets for cancer therapy? *Nat. Rev. Cancer* **10**, 842–857 (2010).
5. H. Ledford, Cancer: The Ras renaissance. *Nature* **520**, 278–280 (2015).
6. E. F. Pai *et al.*, Structure of the guanine-nucleotide-binding domain of the Ha-ras oncogene product p21 in the triphosphate conformation. *Nature* **341**, 209–214 (1989).
7. M. V. Milburn *et al.*, Molecular switch for signal transduction: Structural differences between active and inactive forms of proto-oncogenic ras proteins. *Science* **247**, 939–945 (1990).
8. J. M. L. Ostrem, K. M. Shokat, Direct small-molecule inhibitors of KRAS: From structural insights to mechanism-based design. *Nat. Rev. Drug Discov.* **15**, 771–785 (2016).
9. S. Lu *et al.*, Ras conformational ensembles, allostery, and signaling. *Chem. Rev.* **116**, 6607–6665 (2016).
10. H. R. Kalbitzer *et al.*, Intrinsic allosteric inhibition of signaling proteins by targeting rare interaction states detected by high-pressure NMR spectroscopy. *Angew. Chem. Int. Ed. Engl.* **52**, 14242–14246 (2013).
11. Y. Mao, H. Yao, H. Wang, P. Cheng, D. Long, Microsecond timescale dynamics of GDP-bound ras underlies the formation of novel inhibitor-binding pockets. *Angew. Chem. Int. Ed. Engl.* **55**, 15629–15632 (2016).
12. M. Geyer *et al.*, Conformational transitions in p21ras and in its complexes with the effector protein Raf-RBD and the GTPase activating protein GAP. *Biochemistry* **35**, 10308–10320 (1996).
13. H. R. Kalbitzer, M. Spoerner, P. Ganser, C. Hozsa, W. Kremer, Fundamental link between folding states and functional states of proteins. *J. Am. Chem. Soc.* **131**, 16714–16719 (2009).
14. M. Araki *et al.*, Solution structure of the state 1 conformer of GTP-bound H-Ras protein and distinct dynamic properties between the state 1 and state 2 conformers. *J. Biol. Chem.* **286**, 39644–39653 (2011).
15. C. O'Connor, E. L. Kovrigin, Global conformational dynamics in ras. *Biochemistry* **47**, 10244–10246 (2008).
16. X. Chen *et al.*, Extending the lifetime of native GTP-bound ras for site-resolved NMR measurements: Quantifying the allosteric dynamics. *Angew. Chem. Int. Ed. Engl.* **58**, 2730–2733 (2019).
17. F. Shima *et al.*, Structural basis for conformational dynamics of GTP-bound Ras protein. *J. Biol. Chem.* **285**, 22696–22705 (2010).
18. D. Liu, X. Chen, D. Long, NMR-derived conformational ensemble of state 1 of activated ras reveals insights into a druggable pocket. *J. Phys. Chem. Lett.* **11**, 3642–3646 (2020).
19. M. Spoerner, C. Herrmann, I. R. Vetter, H. R. Kalbitzer, A. Wittinghofer, Dynamic properties of the Ras switch I region and its importance for binding to effectors. *Proc. Natl. Acad. Sci. U.S.A.* **98**, 4944–4949 (2001).
20. F. Shima *et al.*, In silico discovery of small-molecule Ras inhibitors that display antitumor activity by blocking the Ras-effector interaction. *Proc. Natl. Acad. Sci. U.S.A.* **110**, 8182–8187 (2013).
21. M. J. Smith, B. G. Neel, M. Ikura, NMR-based functional profiling of RASopathies and oncogenic RAS mutations. *Proc. Natl. Acad. Sci. U.S.A.* **110**, 4574–4579 (2013).
22. J. M. Ostrem, U. Peters, M. L. Sos, J. A. Wells, K. M. Shokat, K-Ras(G12C) inhibitors allosterically control GTP affinity and effector interactions. *Nature* **503**, 548–551 (2013).
23. Q. Sun *et al.*, Discovery of small molecules that bind to K-Ras and inhibit Sos-mediated activation. *Angew. Chem. Int. Ed. Engl.* **51**, 6140–6143 (2012).
24. T. Maurer *et al.*, Small-molecule ligands bind to a distinct pocket in Ras and inhibit SOS-mediated nucleotide exchange activity. *Proc. Natl. Acad. Sci. U.S.A.* **109**, 5299–5304 (2012).
25. J. A. Maier *et al.*, ff14SB: Improving the accuracy of protein side chain and backbone parameters from ff99SB. *J. Chem. Theory Comput.* **11**, 3696–3713 (2015).
26. A. Abragam, *The Principles of Nuclear Magnetism* (Clarendon Press, 1961).
27. M. W. F. Fischer, A. Majumdar, E. R. P. Zuiderweg, Protein NMR relaxation: Theory, applications and outlook. *Prog. Nucl. Magn. Reson. Spectrosc.* **33**, 207–272 (1998).
28. Y. Shen, A. Bax, SPARTA+: A modest improvement in empirical NMR chemical shift prediction by means of an artificial neural network. *J. Biomol. NMR* **48**, 13–22 (2010).
29. P. J. Kraulis, P. J. Domaille, S. L. Campbell-Burk, T. Van Aken, E. D. Laue, Solution structure and dynamics of ras p21.GDP determined by heteronuclear three- and four-dimensional NMR spectroscopy. *Biochemistry* **33**, 3515–3531 (1994).
30. S. Xu *et al.*, Structural insight into the rearrangement of the switch I region in GTP-bound G12A K-Ras. *Acta Crystallogr. D Struct. Biol.* **73**, 970–984 (2017).
31. M. Rueda *et al.*, A consensus view of protein dynamics. *Proc. Natl. Acad. Sci. U.S.A.* **104**, 796–801 (2007).
32. D. W. Li, R. Brüschweiler, All-atom contact model for understanding protein dynamics from crystallographic B-factors. *Biophys. J.* **96**, 3074–3081 (2009).
33. R. F. Tilton Jr, J. C. Dewan, G. A. Petsko, Effects of temperature on protein structure and dynamics: X-ray crystallographic studies of the protein ribonuclease-A at nine different temperatures from 98 to 320 K. *Biochemistry* **31**, 2469–2481 (1992).
34. Y. Xue, N. R. Skrynnikov, Ensemble MD simulations restrained via crystallographic data: Accurate structure leads to accurate dynamics. *Protein Sci.* **23**, 488–507 (2014).
35. D. E. Koshland, Application of a theory of enzyme specificity to protein synthesis. *Proc. Natl. Acad. Sci. U.S.A.* **44**, 98–104 (1958).
36. C. J. Tsai, B. Ma, R. Nussinov, Folding and binding cascades: Shifts in energy landscapes. *Proc. Natl. Acad. Sci. U.S.A.* **96**, 9970–9972 (1999).
37. D. D. Boehr, R. Nussinov, P. E. Wright, The role of dynamic conformational ensembles in biomolecular recognition. *Nat. Chem. Biol.* **5**, 789–796 (2009).
38. G. G. Hammes, Y. C. Chang, T. G. Oas, Conformational selection or induced fit: A flux description of reaction mechanism. *Proc. Natl. Acad. Sci. U.S.A.* **106**, 13737–13741 (2009).
39. K. G. Daniels, Y. Suo, T. G. Oas, Conformational kinetics reveals affinities of protein conformational states. *Proc. Natl. Acad. Sci. U.S.A.* **112**, 9352–9357 (2015).
40. M. R. Janes *et al.*, Targeting KRAS mutant cancers with a covalent G12C-specific inhibitor. *Cell* **172**, 578–589.e17 (2018).
41. R. Hansen *et al.*, The reactivity-driven biochemical mechanism of covalent $KRAS^{G12C}$ inhibitors. *Nat. Struct. Mol. Biol.* **25**, 454–462 (2018).
42. M. Zeng *et al.*, Potent and selective covalent quinazoline inhibitors of KRAS G12C. *Cell Chem. Biol.* **24**, 1005–1016.e3 (2017).

43. C. I. Nnadi *et al*., Novel K-ras G12C switch-II covalent binders destabilize Ras and accelerate nucleotide exchange. *J. Chem. Inf. Model.* **58**, 464–471 (2018).
44. M. M. Mysinger, M. Carchia, J. J. Irwin, B. K. Shoichet, Directory of useful decoys, enhanced (DUD-E): Better ligands and decoys for better benchmarking. *J. Med. Chem.* **55**, 6582–6594 (2012).
45. F. McCormick, Progress in targeting RAS with small molecule drugs. *Biochem. J.* **476**, 365–374 (2019).
46. A. T. Brünger *et al*., Crystal structure of an active form of RAS protein, a complex of a GTP analog and the HRAS p21 catalytic domain. *Proc. Natl. Acad. Sci. U.S.A.* **87**, 4849–4853 (1990).
47. O. F. Lange *et al*., Recognition dynamics up to microseconds revealed from an RDC-derived ubiquitin ensemble in solution. *Science* **320**, 1471–1475 (2008).
48. Y. Shen *et al*., Consistent blind protein structure generation from NMR chemical shift data. *Proc. Natl. Acad. Sci. U.S.A.* **105**, 4685–4690 (2008).
49. G. Nodet *et al*., Quantitative description of backbone conformational sampling of unfolded proteins at amino acid resolution from NMR residual dipolar couplings. *J. Am. Chem. Soc.* **131**, 17908–17918 (2009).
50. D. M. Korzhnev, T. L. Religa, W. Banachewicz, A. R. Fersht, L. E. Kay, A transient and low-populated protein-folding intermediate at atomic resolution. *Science* **329**, 1312–1316 (2010).
51. V. Tugarinov, V. Kanelis, L. E. Kay, Isotope labeling strategies for the study of high-molecular-weight proteins by solution NMR spectroscopy. *Nat. Protoc.* **1**, 749–754 (2006).
52. M. R. Hansen, L. Mueller, A. Pardi, Tunable alignment of macromolecules by filamentous phage yields dipolar coupling interactions. *Nat. Struct. Biol.* **5**, 1065–1074 (1998).
53. M. Rückert, G. Otting, Alignment of biological macromolecules in novel nonionic liquid crystalline media for NMR experiments. *J. Am. Chem. Soc.* **122**, 7793–7797 (2000).
54. J. J. Chou, S. Gaemers, B. Howder, J. M. Louis, A. Bax, A simple apparatus for generating stretched polyacrylamide gels, yielding uniform alignment of proteins and detergent micelles. *J. Biomol. NMR* **21**, 377–382 (2001).